



1 Hemispherically asymmetric volcanic forcing of tropical hydroclimate and water  
2 isotopologue variability during the last millennium

3

4 **Christopher M. Colose<sup>1</sup>, Allegra N. LeGrande<sup>2</sup>, Mathias Vuille<sup>1</sup>**

5

6 [1] Dept. of Atmospheric & Environmental Sciences, University at Albany, SUNY,

7 Albany, NY 12222

8 [2] NASA Goddard Institute for Space Studies, New York, NY, 10025

9 Correspondence to: Christopher Colose (ccolose@albany.edu)



10 **Abstract**

11 Volcanic aerosols exert the most important natural radiative forcing of the last  
12 millennium. State-of-the-art paleoclimate simulations of this interval are typically forced  
13 with diverse spatial patterns of volcanic forcing, leading to different responses in tropical  
14 hydroclimate. Recently, theoretical considerations relating the intertropical convergence  
15 zone (ITCZ) position to the demands of global energy balance have emerged in the  
16 literature, allowing for a connection to be made between the paleoclimate simulations and  
17 recent developments in the understanding of ITCZ dynamics. These energetic  
18 considerations aid in explaining the well-known historical, paleoclimatic, and modeling  
19 evidence that the ITCZ migrates away from the hemisphere that is energetically deficient  
20 in response to asymmetric forcing.

21 Here we use two separate general circulation model (GCM) suites of experiments  
22 for the Last Millennium to relate the ITCZ position to asymmetries in prescribed volcanic  
23 sulfate aerosols in the stratosphere and related asymmetric radiative forcing. We discuss  
24 the ITCZ shift in the context of atmospheric energetics, and discuss the ramifications of  
25 transient ITCZ migrations for other sensitive indicators of changes in the tropical  
26 hydrologic cycle, including global streamflow. For the first time, we also offer insight  
27 into the large-scale fingerprint of water isotopologues in precipitation ( $\delta^{18}\text{O}_p$ ) in response  
28 to asymmetries in radiative forcing.

29 The ITCZ shifts away from the hemisphere with greater forcing. Since the  
30 isotopic composition of the ITCZ is relatively depleted compared to areas outside this  
31 zone, this meridional precipitation migration results in a large-scale enrichment  
32 (depletion) in the isotopic composition of tropical precipitation in regions the ITCZ



33 moves away from (toward). Our results highlight the need for careful consideration of the  
34 spatial structure of volcanic forcing for both impact assessments and for the testing of  
35 models against paleoclimate evidence.



36 **1. Introduction**

37

38 The ITCZ is the narrow belt of deep convective clouds and strong precipitation  
39 that develops in the rising branch of the Hadley circulation. Migrations in the position of  
40 the ITCZ have important consequences for local rainfall availability, drought and river  
41 discharge, and the distribution of water isotopologues (e.g.,  $\delta^{18}\text{O}$  and  $\delta\text{D}$ , hereafter  
42 simply referred to as water isotopes, with notation developed in section 3.3) that are used  
43 to derive inferences of past climate change in the tropics.

44 Meridional displacements of the ITCZ are constrained by requirements of  
45 reaching a consistent energy balance on both sides of the ascending branch of the Hadley  
46 circulation (e.g., Kang et al., 2008, 2009; Schneider et al., 2014). Although the ITCZ is a  
47 convergence zone in near-surface meridional mass flux, it is a divergence zone  
48 energetically. The stratification of the tropical atmosphere is such that moist static energy  
49 (MSE) is greater aloft than near the surface, compelling Hadley cells to transport energy  
50 in the direction of their upper tropospheric flow (Neelin and Held, 1987). If the system is  
51 perturbed with preferred heating or cooling in one hemisphere, the anomalous circulation  
52 that develops resists the resulting asymmetry by transporting energy from the heated to  
53 the cooled hemisphere. Conversely, meridional moisture transport in the Hadley  
54 circulation is primarily confined to the low-level equatorward flow, so the response of the  
55 tropical circulation to asymmetric heating demands an ITCZ migration away from the  
56 hemisphere that is energetically deficient. Since the mean circulation dominates the  
57 atmospheric energy transport (AET) in the vicinity of the equator, the recognition that the  
58 ITCZ is approximately co-located with the latitude where meridional column-integrated



59 energy fluxes vanish, has provided a basis for relating the mean ITCZ position to AET.  
60 We note that this perspective focused on atmospheric energetics is distinct from one that  
61 emphasizes sea surface temperature gradients across the tropics (Maroon et al., 2016, in  
62 press).

63 This energetic framework has emerged as a central paradigm of climate change  
64 problems, providing high explanatory and predictive power for ITCZ migrations across  
65 timescales and forcing mechanisms (Donohoe et al., 2013; McGee et al., 2014; Schneider  
66 et al., 2014). It is also a compelling basis for understanding why the climatological  
67 annual-mean ITCZ resides in the northern hemisphere (NH); it has been shown that this  
68 is associated with ocean heat transport, which in the prevailing climate is directed  
69 northward across the equator (Frierson et al., 2013; Marshall et al., 2014). The energetic  
70 paradigm also predicts an ITCZ response for asymmetric perturbations that arise from  
71 remote extratropical forcing. This phenomenon is exhibited in many numerical  
72 experiments, is borne out paleoclimatically, and has gradually matured in its theoretical  
73 articulation (Chiang and Bitz, 2005; Broccoli et al., 2006; Kang et al., 2008, 2009;  
74 Yoshimori and Broccoli, 2008, 2009; Chiang and Friedman, 2012; Frierson and Hwang,  
75 2012; Bischoff and Schneider, 2014; Adam et al., 2016, in press).

76 Thus far, however, little or only very recent attention has been given to the  
77 relation between transient ITCZ migrations and explosive volcanism (although see Iles et  
78 al., 2014; Liu et al., 2016, section 2). This connection has received recent consideration  
79 using carbon isotopes in paleo-records (Ridley et al., 2015) or in the context of volcanic  
80 and anthropogenic aerosol forcing in the 20th century (Friedman et al., 2013; Hwang et  
81 al., 2013; Allen et al., 2015; Haywood et al., 2015). The purpose of this paper is to use



82 the energetic paradigm as our vehicle for interpreting the climate response in  
83 paleoclimate simulations featuring explosive volcanism of varying spatial structure.

84 Much of the existing literature highlighting the importance of spatial structure in  
85 volcanic forcing focuses on the problem of tropical vs. high-latitude eruptions and  
86 dynamical ramifications of changing pole-to-equator temperature gradients (e.g., Robock,  
87 2000; Stenchikov et al., 2002; Shindell et al., 2004; Oman et al., 2005, 2006; Kravitz  
88 and Robock, 2011), which is a distinct problem from one focused on inter-hemispheric  
89 asymmetries the volcanic forcing. Furthermore, episodes with preferentially higher  
90 aerosol loading in the southern hemisphere (SH) have received comparatively little  
91 attention, probably due to the greater propensity for both natural or anthropogenic aerosol  
92 forcing to be skewed toward the NH.

93 Here we show that it matters greatly over which hemisphere the aerosol loading is  
94 concentrated and that this asymmetry in aerosol forcing has a first-order impact on  
95 changes in the tropical hydrologic cycle, atmospheric energetics, and the distribution of  
96 the isotopic composition of precipitation.

97

## 98 **2. Methods**

99

100 To illuminate how the spatial structure of volcanic forcing expresses itself in the  
101 climate system, we call upon two state-of-the-art models that were run over the pre-  
102 industrial part of the last millennium (LM), nominally 850-1850 C.E., the most recent  
103 key interval identified by the Paleoclimate Model Intercomparison Project Phase 3  
104 (PMIP3). An analysis of this time period is motivated by the fact that volcanic forcing is



105 the most important radiative perturbation during the LM (LeGrande and Anchukaitis,  
106 2015; Atwood et al., 2016). Furthermore, the available input data that defines volcanic  
107 forcing in CMIP5/PMIP3 feature a greater sample of events, larger radiative excursions,  
108 and richer diversity in their spatial structure than is available over the historical period.  
109 This allows for a robust composite analysis to be performed over this interval.

110 The two GCM's that we use as our laboratory are NASA GISS ModelE2-R  
111 (hereafter, GISS-E2) and the Community Earth System Model Last Millennium  
112 Ensemble (CESM LME, hereafter, just CESM). The GISS-E2 version used here is the  
113 same as the non-interactive atmospheric composition (NINT) physics version used in the  
114 CMIP5 initiative (Miller et al., 2014). CESM is a community resource that became  
115 available in 2015 (Otto-Bliesner et al., 2016, in press), employing version 1.1 of CESM  
116 that consists of several component models each representing different aspects of the Earth  
117 system; the atmospheric component is the Community Atmosphere Model version 5  
118 (CAM5, see Hurrell et al., 2013), which in CESM features 1.9° latitude x 2.5° longitude  
119 horizontal resolution with 30 vertical levels up to ~2 hPa. The GISS-E2 model is run at a  
120 comparable horizontal resolution (2° x 2.5°) and with 40 vertical levels up to 0.1 hPa.

121 Both GISS-E2 and CESM feature multiple ensemble members that include  
122 volcanic forcing, which is one of the motivations for our model choices, since our  
123 different volcanic composites (see below) each sample a limited number of events within  
124 the LM. There are 15 members in CESM, including ten with all transient forcings during  
125 the LM and five volcano-only simulations. This number is much higher than the number  
126 of ensembles used for participating LM simulations in CMIP5/PMIP3. The volcanic  
127 reconstruction is based on Gao et al., 2008 (G08) and the ensemble spread is generated



128 from round off differences in the initial atmospheric state ( $\sim 10^{-14}$  °C changes in the  
129 temperature field). Sampling many realizations of internal variability is critical in the  
130 context of volcanic eruptions given the different trajectories that can arise in the  
131 atmosphere-ocean system in response to a similar forcing (Deser et al., 2012). For GISS-  
132 E2, there exist six available members that include a transient volcanic forcing history.  
133 Here, however we use only the three simulations that utilize the G08 reconstruction. This  
134 is done in order to composite over the same dates as the CESM events, as well as the fact  
135 that the other volcanic forcing dataset that NASA explored in their suite of simulations  
136 (Crowley and Unterman, 2013) only provides data over four latitude bands, complicating  
137 inferences concerning hemispheric asymmetry. The three GISS-E2 members also differ  
138 in the combination of transient solar/land-use histories employed, but since our analysis  
139 focuses only on the immediate post-volcanic imprint, the impact of these smaller  
140 amplitude and slowly varying forcings is very small. Taken together, there are 18,000  
141 years of simulation time in which to explore the post-volcanic response while probing  
142 both initial condition sensitivity and the structural uncertainty between two different  
143 models.

144 In both GISS-E2 and CESM, the model response is a slave to the spatial  
145 distribution of the imposed radiative forcing, which was based on the aerosol transport  
146 model of G08, rather than the coupled model stratospheric wind field, thus losing  
147 potential insight into the seasonal dependence of the response that may arise in the real  
148 world. For our purpose, however, this is a more appropriate experimental setup, since the  
149 spatial structure of the forcing is implicitly known (Figure 1).



150           In CESM, aerosols are treated as a fixed size distribution in three levels of the  
151 stratosphere, which provide a radiative effect, including shortwave scattering and  
152 longwave absorption. The GISS-E2 model is forced with prescribed Aerosol Optical  
153 Depth (AOD) from 15-35 km, based on a linear scaling with the G08-derived column  
154 volcanic aerosol mass (Stothers, 1984; Schmidt et al., 2011), with a size distribution as a  
155 function of AOD as in Sato et al (1993) – thus altering the relative long wave and  
156 shortwave forcing (Lacis et al, 1992; Lacis, 2015). The stratospheric sulfate  
157 aerosol loadings given by G08 are a function of latitude, altitude and month.

158           We note that the GISS-E2 runs forced with the G08 reconstruction in  
159 CMIP5/PMIP3 were mis-scaled to give approximately twice the appropriate AOD  
160 forcing, although the spatial structure of forcing in the model is still coherent with G08.  
161 For this reason, we emphasize the CESM results in this study. However, we still choose  
162 to examine the results from the GISS-E2 model for two reasons. First, we view this error  
163 as an opportunity to explore the climate response to a wider range of hemispheric forcing  
164 gradients, even though it comes at the expense of not being able to relate the results to  
165 actual events during the LM. Secondly, the GISS-E2 LM runs were equipped with  
166 interactive water isotopes (section 3.3). A self-consistent simulation of the isotope field in  
167 a GCM is important, since it removes a degree of uncertainty in the error-prone  
168 conversion of isotopic signals into more fundamental climate variables. To our  
169 knowledge, an explicit simulation of the isotopic distribution following asymmetries in  
170 volcanic forcing has not previously been reported.

171           In our analysis, we classify volcanic events as “symmetric” (SYMM), and  
172 “asymmetric” (ASYMM<sub>X</sub>), where the subscript X refers to a preferred forcing in the



173 Northern Hemisphere (NH) or Southern Hemisphere (SH). Composites are formed from  
174 all events within each of the three classifications in order to isolate the volcanic signal.  
175 All events must have a global aerosol loading  $> 8 \text{ Tg}$  (1 teragram =  $10^{12} \text{ g}$ ) averaged  
176 over at least one five-month period to qualify as an eruption and enter the composite.  
177 Events fall into the SYMM category if they have less than a 25% difference in aerosol  
178 loading between hemispheres, while the ASYMM<sub>NH</sub> events have an at least 25% higher  
179 loading in the NH relative to the SH. The opposite applies to events falling into the  
180 ASYMM<sub>SH</sub> category. The dates for which these thresholds are satisfied are taken from  
181 the original G08 dataset (Table 1), and thus the CESM and GISS-E2 composites are  
182 formed using the same events despite the GISS-E2 mis-scaling and other differences in  
183 model implementation.

184 Results are reported for the boreal warm season (averaged over the MJJAS  
185 months) and cold season (NDJFM). For each eruption, we identify the post-volcanic  
186 response by averaging the number of consecutive seasons during which the above criteria  
187 are met, typically 1-3 years. All seasons for an eruption lasting more than one year are  
188 first averaged together to avoid over-weighting its influence in the composite. We use the  
189 previous five seasons as a reference period to calculate an anomaly for each event. For  
190 overlapping eruptions, the five years prior to the first eruption are used instead. This  
191 relatively short reference period allows creating composites that are unaffected by  
192 changes in the mean background state due to low-frequency climate change during the  
193 LM. Composites for the SYMM, ASYMM<sub>NH</sub>, and ASYMM<sub>SH</sub> cases are then obtained for  
194 each season and model by averaging over all anomaly fields within the appropriate  
195 classification, including all ensemble members. A two-sided Student's t-test was applied



196 to all composites in order to identify regions where the anomalous signal is significantly  
197 different ( $p < 0.05$ ) from the mean background conditions.

198 In no case does the classification of a given eruption change over the duration of  
199 the event, with the exception of the largest eruption (Samalas, 1258 C.E.), which  
200 straddles the 25% asymmetry criterion throughout the years following the event. This  
201 eruption would project itself most strongly onto the symmetric results but may reasonably  
202 be classified as  $ASYMM_{NH}$  due to the greater absolute aerosol loadings in the NH. Due to  
203 this ambiguity, we omit the Samalas event from our main results. We note that there are  
204 far more asymmetric eruptions during the LM based on our criteria than SYMM cases,  
205 most of which easily meet the two thresholds outlined above. Because of this, the  
206 classification assigned to each event is quite robust to slightly different criteria in  
207 defining the ratio (or differences) in hemispheric aerosol loading. Since the asymmetric  
208 composites are formed from a relatively large number of events, our results are  
209 insensitive to the addition or removal of individual eruptions that may be more  
210 ambiguous in their degree of asymmetry. However, the SYMM composites are formed  
211 from only a few events, and are therefore more sensitive to each of the individual  
212 eruptions that are included.

213 We stress that in this study we are agnostic concerning the actual location of  
214 individual LM eruptions. Although aerosols from high-latitude eruptions tend to be  
215 confined to the hemisphere in which the eruption occurs, tropical eruptions may also lead  
216 to an asymmetric aerosol forcing, as happened during the eruptions of El Chichón and  
217 Mt. Agung during the historical period. The G08 reconstructions used a simple transport  
218 model that does not allow for cross-equatorial aerosol transport, and the inferred



219 asymmetry may not be coherent with other reconstructions (e.g., the Tambora eruption in  
220 1815 features more aerosols in the SH than in the NH in the Crowley and Unterman  
221 (2013) reconstruction, which is not the case in G08). The timing and magnitude of LM  
222 eruptions is an important topic of research (see e.g., updates from Sigl et al., 2015), but  
223 our composite should strictly be interpreted as a self-consistent response to the imposed  
224 forcing in the model.

225         Similar approaches of stratifying volcanic events during the LM have only begun  
226 to emerge in the literature (e.g., Liu et al., 2016). Iles and Hegerl (2015) showed the  
227 CMIP5 multi-model mean precipitation response to a few post-1850 eruptions,  
228 emphasizing the spatial structure of the aerosols (see their supplementary S14) but noted  
229 that it would be desirable for a greater sample of events in order to group by the location  
230 of the aerosol cloud. The LM provides an appropriate setting for this. Additionally, we  
231 add to these results by presenting a simulation of the water isotope distribution following  
232 different volcanic excursions. We emphasize that we are screening events by spatial  
233 structure and since different magnitude eruptions enter into the different composites, a  
234 quantitative comparison of the different event classifications (or the two models) is not  
235 our primary objective and would require a more controlled experiment. Instead, we are  
236 reporting on the different composite responses as they exist in current LM simulations,  
237 and highlight the emergent structure that arises from different choices in how eruptions  
238 are sorted, much of which is shown to be scalable to different eruption sizes and robust to  
239 choices of model implementation.

240

### 241 **3. Results**



242

243 *3.1) Temperature, Precipitation and ENSO response*

244

245 Figure 2 illustrates the composite temperature anomaly for each classification and  
246 season in the CESM model. In both the ASYMM<sub>NH</sub> and ASYMM<sub>SH</sub> cases, the  
247 hemisphere that is subjected to the strongest forcing is preferentially cooled. In the  
248 ASYMM<sub>NH</sub> and SYMM results, the cooling peaks over the Eurasian and North American  
249 continents. As expected, there tends to be a much larger response over land, as well as  
250 evidence of NH winter warming in the mid-latitudes, a phenomenon previously  
251 highlighted in the literature and often associated with increased (decreased) pole-to-  
252 equator stratospheric (mid-tropospheric) temperature gradients (Figure S1) and a positive  
253 mode of the Arctic/North Atlantic Oscillation (Robock and Mao, 1992, 1995;  
254 Stenchikov et al., 2002; Shindell et al., 2004; Ortega et al., 2015). This effect is weak in  
255 the ASYMM<sub>NH</sub> composite, likely because the maximal radiative forcing is located in the  
256 NH, offsetting any dynamical response, and is present in the SYMM and ASYMM<sub>SH</sub>  
257 composites in both models (see Figure S2 for the GISS-E2 composite).

258 In the SH, cooling is muted by larger heat capacity associated with smaller land  
259 fraction, with weak responses over the Southern Ocean while still exhibiting statistically  
260 significant cooling in South America, South Africa, and Australia in all cases. In fact, the  
261 cooling in the ASYMM<sub>SH</sub> composites is largely confined to the tropics, in contrast to the  
262 polar amplified pattern that is common to most climate change experiments. The cooling  
263 in all categories is communicated vertically (Figure S1) and across the free tropical



264 troposphere, suggesting AET away from the forced hemisphere (section 3.4) for  
265 asymmetric forcing.

266 The cooling in the GISS-E2 model (Figure S2), displays a very similar spatial  
267 structure to CESM in all categories but with much greater amplitude due to the larger  
268 forcing. We note that the composite-mean forcing that these results are consistent with, is  
269 similar between the four asymmetric panels, but larger in the symmetric cases. In Figure  
270 3, we show the hemispheric and global average temperature response for both models  
271 after normalizing each event by a common global aerosol mass excursion, thereby  
272 accounting for differences in the average forcing among the different eruptions. The  
273 gross features of the hemispheric contrast and reduction in global-mean temperature are  
274 shared between both models.

275 The CESM precipitation response is shown in Figure 4 (Figure S3 for GISS-E2).  
276 For both the ASYMM<sub>NH</sub> and ASYMM<sub>SH</sub> cases, the ITCZ shows a robust displacement  
277 away from the forced hemisphere. The precipitation reduction in the SYMM composites  
278 is much less zonally coherent, instead featuring tropical-mean reductions in precipitation  
279 and a slight increase toward the subtropics (see also Iles et al., 2013; Iles and Hegerl,  
280 2014). Despite global cooling and reduced global evaporation (not shown), the ITCZ shift  
281 in ASYMM<sub>NH</sub> and ASYMM<sub>SH</sub> may result in precipitation increases in the hemisphere  
282 that is least forced (Figure 5), since the precipitation signal is strongest moving with the  
283 ITCZ and because the area-weighted averages emphasize the tropics more than higher  
284 latitudes.

285 The ensemble spread in precipitation for a selected eruption (1762 C.E., NDJFM)  
286 is shown in Figure S4, corresponding to the Icelandic Laki aerosol loading (a large



287 ASYMM<sub>NH</sub> event). We note that the Laki eruption in Iceland actually occurred in 1783  
288 C.E., but is earlier in our composite due to an alignment error in the first version of the  
289 G08 dataset. Results are shown for the 1763 C.E. boreal winter only (the full composite  
290 also includes 1762, see Table 1; Figure S4 also reports the winter 1763 Niño 3.4 anomaly  
291 in surface temperature for each ensemble member, and therefore we restrict the  
292 anomalous precipitation field to a single season). The ITCZ shift away from the NH is  
293 fairly robust across the ensemble members, particularly in the Atlantic basin, although  
294 internal variability still leads to large differences in the spatial pattern of precipitation,  
295 notably in the central and eastern Pacific.

296 The monthly time-evolution of the composite temperature and precipitation  
297 responses for the ASYMM<sub>NH</sub> and ASMM<sub>SH</sub> cases can be viewed in an animation. The  
298 global and hemispheric difference in aerosol loadings is also shown for each monthly  
299 timestep. When averaged over the individual eruptions within each classification, the  
300 global aerosol mass loading remains elevated above 8 Tg for nearly two years, coincident  
301 with the peak temperature and precipitation response that begin to dampen out gradually.  
302 The seasonal migration the monthly precipitation anomaly occurs in nearly the same  
303 sense as the meridional movement in climatological rainfall.

304 In both CESM and GISS-E2, the ITCZ shift is approximately scalable to eruption  
305 size. For both models, we define a precipitation asymmetry index,  $PAi$  (Hwang and  
306 Frierson, 2013) in each season as the area-weighted NH tropical precipitation minus SH  
307 tropical precipitation (extending to 20° latitude) normalized by the model tropical-mean  
308 precipitation, i.e.,

309



$$PAi = \frac{P_{EQ-20^{\circ}N} - P_{20^{\circ}S-EQ}}{P_{20^{\circ}S-20^{\circ}N}} \quad (1)$$

310

311           Supplementary Figure S5 illustrates the relationship between  $PAi$  and the AOD  
312 gradient between hemispheres (AOD is inferred for the CESM model by dividing the  
313 aerosol loading by 75 Tg in each hemisphere, an approximate conversion factor to  
314 compare the results with GISS-E2). The mis-scaling in GISS-E2 results in a wider range  
315 of AOD gradients than occurs in CESM. Both models feature more tropical precipitation  
316 in the NH (SH) during boreal summer (winter) in their climatology, with more  
317 asymmetry in CESM during boreal summer. Interestingly, the most asymmetric events in  
318 GISS-E2 (those that result in equatorward precipitation movements) can be sufficient to  
319 produce more precipitation in the tropical winter hemisphere, thus competing with the  
320 seasonal insolation cycle in determining the seasonal precipitation distribution.

321           The meridional ITCZ shift leads to a number of important tropical climate  
322 responses. For example, an intriguing feature of the temperature pattern in Figure 2 is the  
323 El Niño response that is unique to the  $ASYMM_{NH}$  composites. This is unlikely to be a  
324 residual feature of unforced variability, since there are 240 events in the  $ASYMM_{NH}$   
325 composites (eruptions in Table 1, multiplied by 15 ensemble members), significantly  
326 more than in the other categories. The GISS-E2 temperature composite (Fig. S2) also  
327 features a relatively weak cooling for  $ASYMM_{NH}$ , despite the very large radiative  
328 forcing. This finding is consistent with recent results (Pausata et al., 2015) that found an  
329 El Niño tendency to arise from a Laki-like forcing (in that study, a sequence of aerosol  
330 pulses in the high latitudes that was confined to the NH extratropics). Pausata et al.  
331 (2015) attributed the El Niño development directly to a southward ITCZ displacement.



332 Since low-level converging winds are weak in the vicinity of the ITCZ, a southward  
333 ITCZ displacement leads to weaker easterly winds (a westerly anomaly) across the  
334 central equatorial Pacific. This was shown for a different model (NorESM1-M) and  
335 experimental setup, but also emerges in the ASYMM<sub>NH</sub> composite results for CESM.  
336 Indeed, a composite anomaly of  $\sim 0.5^{\circ}\text{C}$  emerges over the Niño 3.4 domain, lasting up to  
337 two years (Figure S6) with peak anomalies in the first two boreal winters after an  
338 eruption. In addition a relaxation of the zonal winds and re-distribution of water mass  
339 across the Pacific Ocean can be observed in the ASYMM<sub>NH</sub> composite response (Figure  
340 S7).

341 Since the ITCZ shift is a consequence of differential aerosol loading, we argue  
342 that the El Niño tendency in CESM is a forced response in ASYMM<sub>NH</sub> but otherwise  
343 depends on the state of internal variability concurrent with a given eruption. This explains  
344 why no such ENSO response is associated with the composite SYMM or ASYMM<sub>SH</sub>  
345 categories, although we note that El Niño does tend to develop in response to the Samalás  
346 eruption that was removed from our composite, and would strongly influence the  
347 interpretation of the SYMM results due to the few events sampled (not shown). However,  
348 we also caution that this version of CESM exhibits ENSO amplitudes much larger than  
349 observations, and also features strong El Niño events with amplitudes that are  $\sim 2$  times  
350 larger than strong La Niña events even in non-eruption years. Therefore, we choose not to  
351 further explore the dependence of our results on ENSO phasing.

352

353 3.2) *River outflow*

354



355 An ITCZ shift away from the forced hemisphere will manifest itself in several  
356 other components of the tropical hydroclimate system that are important to consider from  
357 the standpoint of both impacts as well as the development of testable predictions. One  
358 such important component of the hydrologic cycle is global streamflow, a variable that  
359 tends to correlate with excessive or deficient precipitation over a catchment. Rivers are  
360 important for ecosystem integrity, agriculture, industry, power generation, and human  
361 consumption. Streamflow anomalies associated with volcanic forcing in observations and  
362 models have previously been documented for the historical period (Trenberth and Dai,  
363 2007; Iles and Hegerl, 2015), and are a useful variable in the context of monitoring since  
364 they integrate precipitation changes over time. Here, we discuss this variable in the  
365 context of our symmetric and asymmetric composites.

366 The hydrology module of the land-component of CESM simulates surface and  
367 subsurface fluxes of water, which serve as input into the CESM River Transport Model  
368 (RTM). The RTM was developed to route river runoff downstream to the ocean or  
369 marginal seas and enable closure of the hydrologic cycle (Oleson et al., 2010). The RTM  
370 is run on a finer grid ( $0.5^\circ \times 0.5^\circ$ ) than the atmospheric component of CESM.

371 Figure 6 shows the river discharge anomalies in our different forcing categories.  
372 The southward ITCZ shift in ASYMM<sub>NH</sub> results in enhanced discharge in central and  
373 southern South America, especially in the southern Amazon and Parana River networks.  
374 These territories of South America, along with southern Africa and Australia are the  
375 primary regions where land precipitation increases in the tropics for ASYMM<sub>NH</sub>, and the  
376 river flow in these areas tends to increase. Our results are also consistent with Oman et al.  
377 (2006), who argue for a reduced Nile River level (northeastern Africa) following several



378 large high northern latitude eruptions, including Laki and the Katmai (1912 C.E.)  
379 eruption. Their results were viewed through the lens of weakened African and Indian  
380 monsoons associated with reduced land-ocean temperature differences; our composite  
381 results suggest that regional precipitation reductions may also be part of a zonally  
382 coherent precipitation shift.

383 In  $ASYMM_{SH}$ , the ITCZ moves northward, resulting in reduced river flux in the  
384 Amazon sector and increases in the Niger of central/western Africa. Interestingly, the  
385 Nile flow is also reduced in this case, although to a lesser extent, despite very modest  
386 precipitation increases during MJJAS for a southern hemisphere biased aerosol forcing.  
387 There are also modest discharge increases in southern Asia. However, there is simply  
388 very little land in regions where northward ITCZ shifts result in enhanced precipitation,  
389 suggesting less opportunity for increases in discharge to a SH biased eruption. For the  
390 SYMM eruptions, river discharge is reduced nearly everywhere in the tropics, consistent  
391 with the precipitation reductions that occur (Figure 3). The response is weaker or even  
392 reversed in the subtropics, such as in southern South America, where precipitation tends  
393 to increase (Iles and Hegerl, 2015).

394

### 395 3.3) *Water isotopic variability*

396

397 Another important variable that integrates several aspects of the tropical climate  
398 system is the isotopic composition of precipitation. Here, we focus on the relative  
399 abundance of  $^1H_2^{18}O$  versus the more abundant  $^1H_2^{16}O$ , commonly expressed as  $\delta^{18}O$ ,  
400 such that:



401

$$\delta^{18}O_p \equiv \left\{ VSMOW^{-1} \frac{O_{mp}^{18}}{O_{mp}^{16}} - 1 \right\} \times 1000 \quad (2)$$

402

403 where  $O_{mp}^{18}$  and  $O_{mp}^{16}$  are the moles of oxygen isotope in a sample, in our case

404 precipitation (denoted by the subscript mp). Delta values are with respect to the isotopic

405 ratio in a standard sample, the Vienna Standard Mean Ocean Water (VSMOW=

406  $2.005 \times 10^{-3}$ ).

407  $\delta^{18}O_p$  is a variable that is directly obtained from many paleoclimate proxy

408 records. Therefore, rather than relying on a conversion of the local isotope signal to some

409 climate variable, the explicit simulation of isotopic variability is preferred for generating

410 potentially falsifiable predictions concerning the imprint associated with asymmetric

411 volcanic eruptions. Indeed,  $\delta^{18}O_p$  variability is the result of an interaction between

412 multiple scales of motion in the atmosphere, the temperature of air in which the

413 condensate was embedded, and exchange processes operating from source to sink of the

414 parcel deposited at a site.

415 Water isotope tracers have been incorporated into the GISS-E2 model's

416 atmosphere, land surface, sea ice and ocean, and are advected and tracked through every

417 stage of the hydrologic cycle. A fractionation factor is applied at each phase change and

418 all freshwater fluxes are tagged isotopically. Stable isotope results from the lineage of

419 GISS-E2 models have a long history of being tested against observations and proxy

420 records (e.g., Vuille et al., 2003; Schmidt et al., 2007; LeGrande and Schmidt, 2008,

421 2009).



422           Figure 7 shows the  $\delta^{18}O_p$  response in the GISS-E2 model. Seasonal calculations  
423   are weighted by the precipitation amount for each month, although changes in the  
424   seasonality of precipitation are not important in driving our results (not shown). The  
425   literature on mechanistic explanations for isotope variability has a rich history of being  
426   described by several “effects” such as a precipitation amount effect in deep convective  
427   regions or a temperature effect at high latitudes (Dansgaard, 1964; Araguás-Araguás et  
428   al., 2000), so named as to reflect the most important climatic driver of isotopic variability  
429   at a site or climate regime. However, the isotopic response to volcanic eruptions is more  
430   complex than simply a response to one of these effects. The  $\delta^{18}O_p$  spatial pattern in the  
431   tropics is negatively correlated with precipitation changes induced by the ITCZ shift  
432   (Figure S5 for GISS-E2), particularly over the ocean. The meridional movement of the  
433   ITCZ leads to an isotopic signal that is more positive (enriched in heavy isotopes) in the  
434   preferentially forced hemisphere. The hemisphere toward which the ITCZ is displaced on  
435   the other hand experiences increased tropical rainfall and a relative depletion of the heavy  
436   isotope (more negative  $\delta^{18}O_p$ ). Thus, the paleoclimatic fingerprint of asymmetric  
437   volcanic eruptions is characterized by a tropical dipole pattern, with more positive  
438   (negative)  $\delta^{18}O_p$  associated with reduced (increased) rainfall.

439           Over land, South America stands out as exhibiting a palette of isotopic patterns  
440   depending on forcing category and season. The South American monsoon system peaks  
441   in austral summer, and the largest precipitation reductions occur in ASYMM<sub>SH</sub> when the  
442   ITCZ moves northward. There is a dipole pattern, characterized by isotopic enrichment  
443   (depletion) in  $^{18}O$  in the northern (southern) tropics of South America in ASYMM<sub>NH</sub>  
444   during NDJFM, while the opposite pattern emerges in ASYMM<sub>SH</sub>, both associated with



445 Atlantic and east Pacific ITCZ displacements. During the austral winter, South American  
446 precipitation peaks in the northern part of the continent where precipitation is reduced in  
447 both the SYMM and ASYMM<sub>SH</sub> composites, leading to large increase in  $\delta^{18}O_p$ . This is  
448 consistent with recent results in Colose et al. (2016), who used the isotope-enabled GISS-  
449 E2 model to form a composite of all large (AOD > 0.1) LM tropical volcanic events  
450 based on the Crowley and Unterman (2013) dataset. The eruptions analyzed in that study  
451 were smaller in amplitude due to differences in the scaling during implementation, as  
452 well as the fact that G08 tends to have larger volcanic events in the original dataset to  
453 begin with. In regions where tropical South American precipitation does not exhibit very  
454 large changes, such in the NDJFM SYMM composites, temperature may explain much of  
455 the isotopic response, again consistent with findings in Colose et al. (2016).

456

### 457 *3.4) Atmospheric Energetics*

458

459 The overarching purpose of this work was to consider the influence of asymmetric  
460 volcanic forcing on the energetic paradigm outlined in section 1. This framework of  
461 analyzing ITCZ shifts in the context of asymmetric forcing predicts a net AET anomaly  
462 toward the hemisphere that is preferentially forced by explosive volcanism, with anti-  
463 correlated dry and latent energy fluxes both contributing to drive the ITCZ away from the  
464 forced hemisphere. To examine this relationship in CESM, we first write a zonal-mean  
465 energy budget for the atmosphere:

466



$$\begin{aligned} & \frac{1}{2\pi a^2 \cos\phi} \frac{\partial AET}{\partial \phi} \\ & = ASR_{TOA} - OLR_{TOA} + SW_{sfc}^{\uparrow} - SW_{sfc}^{\downarrow} + LW_{sfc}^{\uparrow} - LW_{sfc}^{\downarrow} + LH_{sfc} \\ & + SH_{sfc} + L_f Sn - \frac{1}{g} \int_0^{p_s} \frac{\partial(c_p T + L_v q + k)}{\partial t} dp \quad (3) \end{aligned}$$

467

468 where  $ASR_{TOA}$  is the absorbed solar radiation,  $OLR_{TOA}$  is outgoing longwave  
 469 radiation at the top of the atmosphere (TOA),  $SW_{sfc}^{\downarrow}$  is reflected surface shortwave  
 470 radiation,  $SW_{sfc}^{\uparrow}$  is shortwave received by the surface (sfc),  $LW_{sfc}^{\uparrow}$  is longwave radiation  
 471 emitted (or reflected) by the surface,  $LW_{sfc}^{\downarrow}$  is longwave radiation received by the surface,  
 472  $LH$  is the latent heat flux,  $SH$  is the sensible heat flux,  $Sn$  is snowfall rate,  $q$  is specific  
 473 humidity,  $k$  is kinetic energy,  $\phi$  is latitude,  $a$  is the radius of the Earth,  $T$  is temperature,  
 474  $c_p$  is specific heat capacity,  $L_v$  and  $L_f$  are the latent heats of vaporization and fusion,  $p$  is  
 475 pressure ( $p=p_s$  at the surface), and  $g$  is the acceleration due to gravity. All terms are  
 476 defined positive into the atmosphere, and the subscripts denote top-of-atmosphere (TOA)  
 477 or surface flux (sfc) diagnostics. Equation 3 effectively calculates MSE transport (section  
 478 1) as a residual of energy fluxes in the model.

479 The last term ( $\partial/\partial t$ ) on the right side of equation 3 is the time-tendency term,  
 480 representing storage of energy in the atmosphere (hereafter,  $STOR_L$  and  $STOR_D$  for latent  
 481 and dry energy, respectively. The time-derivative is calculated using finite differencing of  
 482 the monthly-mean fields. The term in the parentheses is the moist enthalpy, or MSE  
 483 minus geopotential energy. The kinetic energy is calculated in this study but is several  
 484 orders of magnitude smaller than other terms, and hereafter is folded into the definition of



485  $STOR_D$ ). The tendency term must vanish on timescales of several years or longer, but is  
486 important in our context. We explicitly write out the snowfall term since CESM (and any  
487 CMIP5 model) does not include surface energy changes associated with snow melt over  
488 the ice-free ocean as part of the latent heat diagnostic, and must be calculated to close the  
489 model energy budget.

490 Integrating yields an expression for the atmospheric heat transport across a  
491 latitude circle:

492

$$AET(\phi) = 2\pi a^2 \int_{-\frac{\pi}{2}}^{\phi} (R_{TOA} + F_{sfc} - STOR_L - STOR_D) \cos \phi \, d\phi \quad (4)$$

493 where we have combined the TOA terms into  $R_{TOA}$  and the snowfall and surface  
494 diagnostics have collapsed into a single variable  $F_{sfc}$ . Similarly, the latent heat flux  $\mathcal{H}_L$   
495 across a latitude circle is:

$$\mathcal{H}_L(\phi) = 2\pi a^2 \int_{-\frac{\pi}{2}}^{\phi} (LH_{sfc} - L_v P - STOR_L) \cos \phi \, d\phi \quad (5)$$

496 where  $P$  is precipitation in  $\text{kg m}^{-2} \text{s}^{-1}$ . We note that transport calculations are  
497 presented for CESM and were done for only 14 ensemble members, since there are  
498 missing output files for the requisite diagnostics in one run.

499 Figure 8a shows the annual-mean climatological northward heat transport in  
500 CESM, as performed by both the atmosphere and ocean, in addition to the latent  
501 component of the atmosphere. The total CESM climatological poleward transport is in  
502 good agreement with observational estimates (e.g., Trenberth and Caron, 2001; Wunsch,  
503 2005; Fasullo and Trenberth, 2008), peaking at  $\sim 5.0$  PW and  $\sim 5.2$  PW in the SH and NH



504 subtropics, respectively (1 petawatt =  $10^{15}$  W). In CESM, the SH receives slightly more  
505 net TOA solar radiation than the NH (by  $\sim 1.3$  W m<sup>-2</sup> in the annual-mean), and the NH  
506 loses slightly more net TOA longwave radiation to space (by  $\sim 0.89$  W m<sup>-2</sup>). However, the  
507 CESM annual ocean heat transport is northward across the equator (Figure 8a, blue line),  
508 keeping the NH warmer than the SH by  $\sim 0.97$  °C. As a consequence, AET is directed  
509 southward across the equator (red line). Moisture makes it more difficult for the tropical  
510 circulation to transport energy poleward, and the transport of moisture in the low-level  
511 equatorward flow is directed northward across the equator and associated with an annual-  
512 mean ITCZ approximately co-located with the atmospheric energy flux equator (EFE),  
513 the latitude where AET vanishes. This arrangement of the tropical climate is consistent  
514 with satellite and reanalysis results for the present climate (Kang and Seager, 2012;  
515 Frierson et al., 2013).

516 In response to asymmetric volcanic forcing, anomalous AET is directed toward  
517 the preferentially forced hemisphere (Figure 8b,c), along the imposed temperature  
518 gradient. Results are shown for the annual-mean AET anomaly in ASYMM<sub>NH</sub> and  
519 ASYMM<sub>SH</sub> for one year beginning with the January after each eruption, although  
520 averaging the first 2-3 years yields similar results with slightly smaller amplitudes. The  
521 equatorial AET (AET<sub>eq</sub>) anomaly averaged over all events and ensemble members for  
522 ASYMM<sub>NH</sub> (ASYMM<sub>SH</sub>) is approximately 0.08 (-0.05) PW, defined positive northward,  
523 with much larger near-compensating dry and latent components. The anomalous moisture  
524 convergence drives the ITCZ shift away from the forced hemisphere. Anomalies in  
525 AET<sub>eq</sub> when considering each unique volcanic event (after averaging over the 14



526 ensemble members) are strongly anti-correlated with changes in the energy flux equator  
527 ( $r = -0.97$ ), the latitude where AET vanishes.

528         The change in cross-equatorial energy transport for the SYMM ensemble/eruption  
529 mean (not shown) does not exhibit the coherence of the asymmetric cases for either AET  
530 or the individual dry and moist components, and in all cases does not emerge from  
531 background internal variability.

532         Quantifying the ITCZ shift is non-trivial, since the precipitation field is less  
533 sharply defined than the EFE, and climate models (including the two discussed here)  
534 exhibit a bimodal tropical precipitation distribution (often called a “double-ITCZ”), often  
535 with one mode of higher amplitude in the NH (centered at 8-9 °N in CESM). However,  
536 despite pervasive biases that still exist in the climatology of tropical precipitation in  
537 CMIP5 (e.g., Oueslati and Bellon, 2015), the anomalous precipitation response is still  
538 coherent and the gross features presented here are in agreement with theoretical  
539 considerations. In our analysis, a movement in the latitude of maximum precipitation is  
540 not found to be a persuasive indicator of our ITCZ shift. In fact, the meridional shift is  
541 better described as a movement in the center of mass of the precipitation distribution,  
542 including changes in the relative amplitude of the two modes (e.g., a heightening of the  
543 SH mode for a southward ITCZ shift). Different metrics to describe the shift in the center  
544 of mass have been presented in the literature (e.g., Frierson and Hwang, 2012; Donohoe  
545 et al., 2013; Adam et al., 2016, in press).

546         Here, we first adopt the precipitation median  $\phi_{\text{med}}$  definition (e.g., Frierson and  
547 Hwang, 2012) defined as the latitude where area-weighted precipitation from 20°S to



548  $\phi_{\text{med}}$  equals the precipitation amount from  $\phi_{\text{med}}$  to  $20^\circ\text{N}$ , i.e., where the following is  
549 satisfied:  
550

$$\int_{20^\circ\text{S}}^{\phi_{\text{med}}} P \cos(\phi) d\phi = \int_{\phi_{\text{med}}}^{20^\circ\text{N}} P \cos(\phi) d\phi \quad (6)$$

551

552 When considering the spread across eruption size (regressing the different events  
553 in all three categories together after averaging over ensemble members) we find a  
554 movement of  $\sim -4.7^\circ$  shift in ITCZ latitude per 1 PW of anomalous  $\text{AET}_{\text{eq}}$ . The sign of  
555 this relationship is a robust property of the present climate system, although it is slightly  
556 higher than other estimates (Donohoe et al., 2013) that analyzed the ITCZ scaling with  
557  $\text{AET}_{\text{eq}}$  to a number of other time periods and forcing mechanisms (not volcanic),  
558 including the seasonal cycle,  $\text{CO}_2$  doubling, Last Glacial Maximum, and mid-Holocene.  
559 It was argued in that paper that the ITCZ is “stiff” in the sense that a large  $\text{AET}_{\text{eq}}$  is  
560 required to move the ITCZ. However, the sensitivity of this relationship may vary  
561 considerably depending on ITCZ metric considered (Figure 9 presents a scaling with  
562 different indices), based on the following equation (Adam et al., 2016, in press):

563

$$\phi_{\text{ITCZ}} = \frac{\int_{20^\circ\text{S}}^{20^\circ\text{N}} \phi (P \cos(\phi))^N d\phi}{\int_{20^\circ\text{S}}^{20^\circ\text{N}} (P \cos(\phi))^N d\phi} \quad (7)$$

564

565 Here,  $N$  controls the weighting given to the modes in the precipitation  
566 distribution, typically moving  $\phi_{\text{ITCZ}}$  toward the precipitation maximum as  $N$  increases but



567 also changing the sensitivity of the ITCZ shift to external forcing. Figure 9 shows the  
568 regression of anomalous  $\phi_{\text{med}}$  and  $\phi_{\text{ITCZ}}$  ( $N = 5$ ) against anomalous  $\text{AET}_{\text{eq}}$  ( $N = 5$  with  
569  $r = -0.93$ ) while  $\phi_{\text{ITCZ}}$  ( $N = 3$ ) yielded the highest correlation ( $r = -0.95$ ) and best follows  
570 a 1:1 line with the EFE. The slope of the relationship between ITCZ location and  $\text{AET}_{\text{eq}}$   
571 may vary by a factor of 4-5 depending on the relationship used, and in our case is  
572 approximately  $-11.7^\circ$  shift in ITCZ latitude per 1 PW of anomalous  $\text{AET}_{\text{eq}}$  using  
573  $\phi_{\text{ITCZ}}$  ( $N = 3$ ). Thus, we interpret our results as suggesting that energetically, it is quite  
574 easy to move the ITCZ. Therefore, probing uncertainties in the spatial structure in forcing  
575 must be of first-order consideration for credible paleoclimate simulations.

576

#### 577 **4. Conclusions**

578

579 In this work, we have examined two models, NASA GISS ModelE2-R and the  
580 recently completed CESM Last Millennium Ensemble, and stratified volcanic events by  
581 their degree of asymmetry between hemispheres. We find a robust ITCZ shift away from  
582 the preferentially forced hemisphere, as a consequence of adjustments in the Hadley  
583 circulation that transports anomalous energy into the cooled hemisphere.

584 An important component of our work was using the GISS-E2 model to explicitly  
585 simulate the oxygen isotopic imprint following major volcanic eruptions with asymmetric  
586 aerosol forcing. The ITCZ shift following asymmetric forcing leads to a more positive  
587 isotopic signal in the tropical regions the ITCZ migrates away from, and a relative  
588 depletion in heavy isotopes in regions the ITCZ migrates to. These results provide a  
589 framework for the search of asymmetric volcanic signals in high-resolution isotopic or



590 other temperature and precipitation sensitive proxy data from the tropics.

591           There is still considerably uncertainty in the timing and magnitude of LM  
592 eruptions. Improvements in particle size representation have been identified as critical  
593 target for improved modeling and comparisons to proxy data (e.g., G. Mann et al., 2015).  
594 Here, we argue that the inter-hemispheric asymmetry of the aerosol forcing also emerges  
595 as being of first-order importance for the expected volcanic response. Future  
596 developments in model-proxy comparisons should probe the uncertainty space not just in  
597 the global-mean radiative forcing and coincident internal variability at the time of the  
598 eruption, but also the spatial structure of the aerosol cloud. For example, simulations that  
599 represent volcanic forcing simply as an equivalent reduction in total solar irradiance at  
600 the TOA are unrealistic and cannot be expected to be faithful to tropical climate proxy  
601 records.

602           We hope this contribution will help motivate the connection between the spatial  
603 structure of volcanic episodes and the expression on tropical hydroclimate as an urgent  
604 paleoclimate target in future studies and model intercomparisons. Such investigation also  
605 calls for high-resolution and accurately dated tropical proxy networks that reach across  
606 hemispheres. Developments in seasonally and annually resolved volcanic reconstructions  
607 from both hemispheres (Sigl et al., 2015) are of considerable importance in such  
608 assessments. Future modeling efforts that are forced with the explicit injection of  
609 volcanic species, while also probing multiple realizations of internal variability that will  
610 dictate the spatio-temporal evolution of the volcanic aerosol, are also urgently required as  
611 a tool for understanding both past and future volcanic impacts.

612



613

614 **Acknowledgments**

615 This study was funded by NOAA C2D2 NA10OAR4310126 and NSF awards AGS-  
616 1003690 and AGS-1303828. We would like to thank NASA GISS-E2 for institutional  
617 support. Computing resources supporting this work were provided by the NASA High-  
618 End Computing (HEC) Program through the NASA Center for Climate Simulation  
619 (NCCS) at Goddard Space Flight Center. We acknowledge the CESM1(CAM5) Last  
620 Millennium Ensemble Community Project and supercomputing resources provided by  
621 NSF/CISL/Yellowstone.

622



623 **Figure Captions**

624 **Figure 1.** Annual-mean Northern Hemisphere minus Southern Hemisphere Aerosol  
625 Loading (Tg) from Gao et al. (2008) in black, and clear-sky net solar radiation ( $\text{W/m}^2$ ) in  
626 CESM LME in red (offset to have zero mean).

627

628 **Figure 2.** CESM spatial composite of temperature anomaly ( $^{\circ}\text{C}$ ) for (top row)  
629  $\text{ASYMM}_{\text{NH}}$ , (middle row)  $\text{ASYMM}_{\text{SH}}$ , and (bottom row) SYMM events, each in (left  
630 column) NDJFM and (right column) MJJAS. Stippling indicates statistical significance  
631 using a two-sided student's t-test ( $p < 0.05$ ).

632

633 **Figure 3.** Box-and-whisker diagrams showing the (red fill) global mean, (green fill) NH  
634 mean, and (blue fill) SH mean temperature anomaly to the  $\text{ASYMM}_{\text{NH}}$ ,  $\text{ASYMM}_{\text{SH}}$ , and  
635 SYMM eruption cases on vertical axis. All events are normalized by a 20 Tg global  
636 loading size. For GISS-E2, loadings were multiplied by a factor of two to approximately  
637 account for the over-inflated forcing prior to analysis. Results shown for the CESM and  
638 GISS-E2 model and for NDJFM and MJJAS, as labeled. Black solid line indicates the  
639 median, box width spans the 25-75% quartiles, and tails span the full interval for all  
640 cases.  $N$ =the number of events used in each category, consistent with the number of listed  
641 events in Table 1 (multiplied by 15 for CESM and 3 for GISS-E2). Bottom panels  
642 (CTRL) show the spread of 100 randomly selected and non-overlapping events averaged  
643 over two seasons (relative to the previous five seasons) in a control run.

644

645 **Figure 4.** As in Figure 2, except for precipitation (mm/day).



646

647 **Figure 5.** As in Figure 3, except for precipitation (mm/day, normalized to 20 Tg in the  
648 forced simulations; mm/day in the control). N (not shown) is the same as in Figure 3.

649

650 **Figure 6.** As in Figures 2 and 4, except for river discharge ( $\text{m}^3/\text{s}$ , or  $10^{-6}$  Sverdrups).

651

652 **Figure 7.** GISS-E2 spatial composite of the oxygen isotope anomaly (per mil) in (top  
653 row) ASYMM<sub>NH</sub>, (middle row) ASYMM<sub>SH</sub>, and (bottom row) SYMM events in (left  
654 column) NDJFM and (right column) MJJAS.

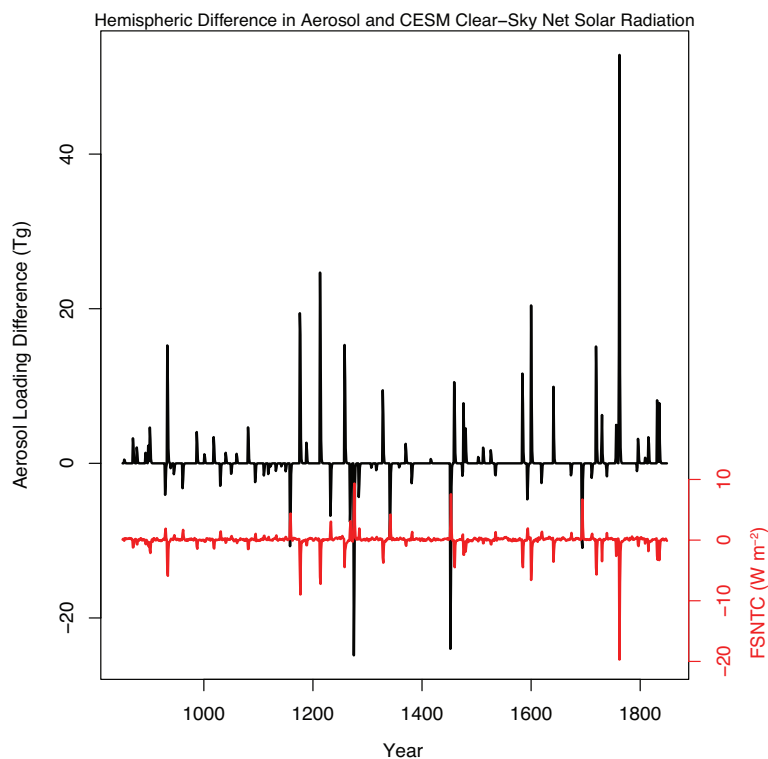
655

656 **Figure 8. a)** CESM climatology of atmosphere+ocean energy transport (PW, black),  
657 atmosphere only (red), ocean only (dark blue), moisture component of the atmosphere  
658 (latent heat, dashed aqua). **b)** Ensemble/Eruption mean anomaly in atmospheric heat  
659 transport for ASYMM<sub>NH</sub> eruptions in total (red), dry (purple), and latent (aqua)  
660 components. Lighter lines associated with the dry and latent components indicate the  
661 eruption spread, each averaged over 14 ensemble members. **c)** As in (b), except for  
662 ASYMM<sub>SH</sub> eruptions. Grey envelope corresponds to the total AET anomaly vs. latitude  
663 in a control simulation using 50 realizations of a composite formed from the same dates  
664 as the ASYMM<sub>NH</sub> results (16 “events” with no external forcing). Vertical bars correspond  
665 to the range of (aqua) latent and (orange) dry components of AET<sub>eq</sub> in the control  
666 composite.

667



668 **Figure 9.** Annual-mean ITCZ shift represented by changes in (topleft)  $\phi_{\text{med}}$  and (topright)  
669  $\phi_{\text{ITCZ}}$  ( $N = 5$ ) vs. change in  $\text{AET}_{\text{eq}}$ . (bottomleft) Changes in  $\phi_{\text{ITCZ}}$  ( $N = 3$ ) vs. change in  
670 EFE. See text for definitions. (bottomright) Total AET vs. latitude for a small band  
671 centered around the equator for all volcanic events in (green)  $\text{ASYMM}_{\text{NH}}$ , (blue)  
672  $\text{ASYMM}_{\text{SH}}$ , and (black) SYMM cases. Black dashed line indicates climatological or pre-  
673 eruption AET values (different choices are indistinguishable). Colored arrows represent  
674 the direction of anomalous  $\text{AET}_{\text{eq}}$ .  
675

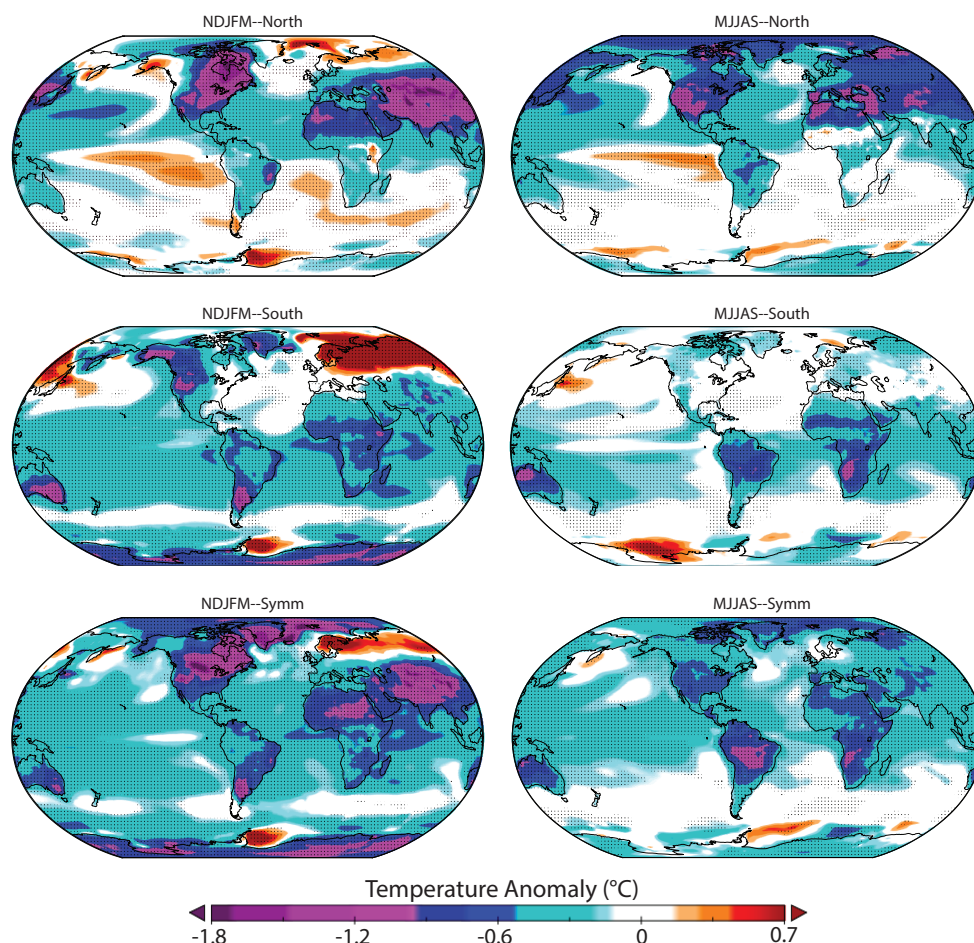


676

677 **Figure 1.** Annual-mean Northern Hemisphere minus Southern Hemisphere Aerosol  
678 Loading (Tg) from Gao et al. (2008) in black, and clear-sky net solar radiation ( $\text{W}/\text{m}^2$ ) in  
679 CESM LME in red (offset to have zero mean).

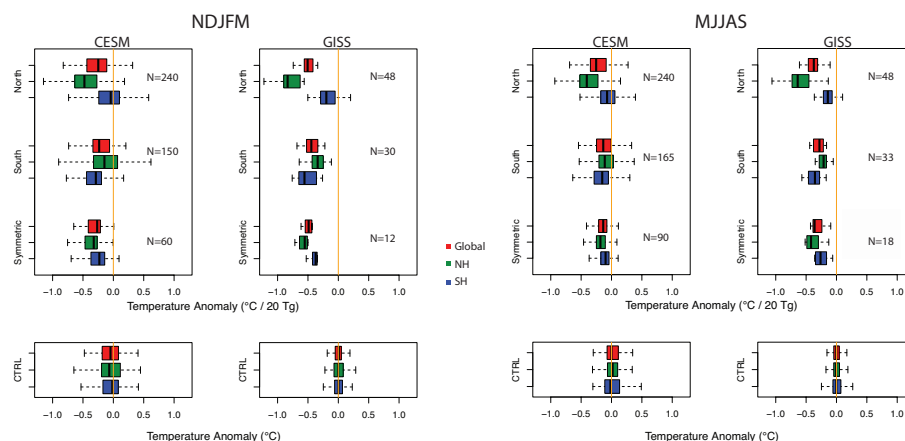


Temperature (Ensemble/Event Mean)



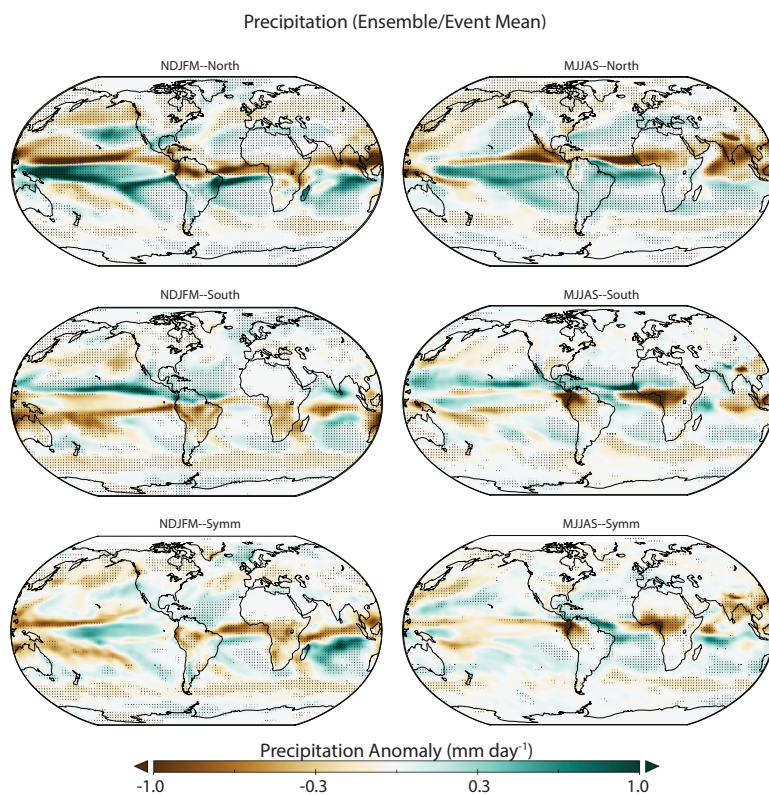
680

681 **Figure 2.** CESM spatial composite of temperature anomaly (°C) for (top row)  
682 ASYMM<sub>NH</sub>, (middle row) ASYMM<sub>SH</sub>, and (bottom row) SYMM events, each in (left  
683 column) NDJFM and (right column) MJJAS. Stippling indicates statistical significance  
684 using a two-sided student's t-test ( $p < 0.05$ ).



685

686 **Figure 3.** Box-and-whisker diagrams showing the (red fill) global mean, (green fill) NH  
 687 mean, and (blue fill) SH mean temperature anomaly to the ASYMM<sub>NH</sub>, ASYMM<sub>SH</sub>, and  
 688 SYMM eruption cases on vertical axis. All events are normalized by a 20 Tg global  
 689 loading size. For GISS-E2, loadings were multiplied by a factor of two to approximately  
 690 account for the over-inflated forcing prior to analysis. Results shown for the CESM and  
 691 GISS-E2 model and for NDJFM and MJJAS, as labeled. Black solid line indicates the  
 692 median, box width spans the 25-75% quartiles, and tails span the full interval for all  
 693 cases. N=the number of events used in each category, consistent with the number of listed  
 694 events in Table 1 (multiplied by 15 for CESM and 3 for GISS-E2). Bottom panels  
 695 (CTRL) show the spread of 100 randomly selected and non-overlapping events averaged  
 696 over two seasons (relative to the previous five seasons) in a control run.



697

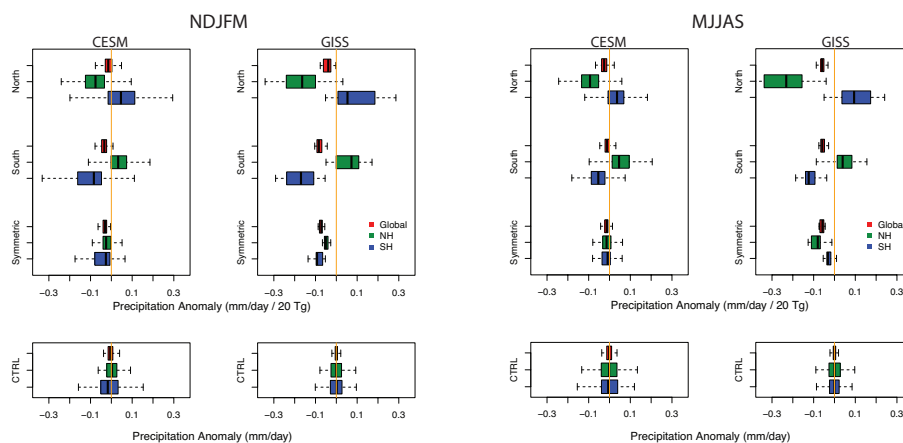
698 **Figure 4.** As in Figure 2, except for precipitation (mm/day).

699

700



701



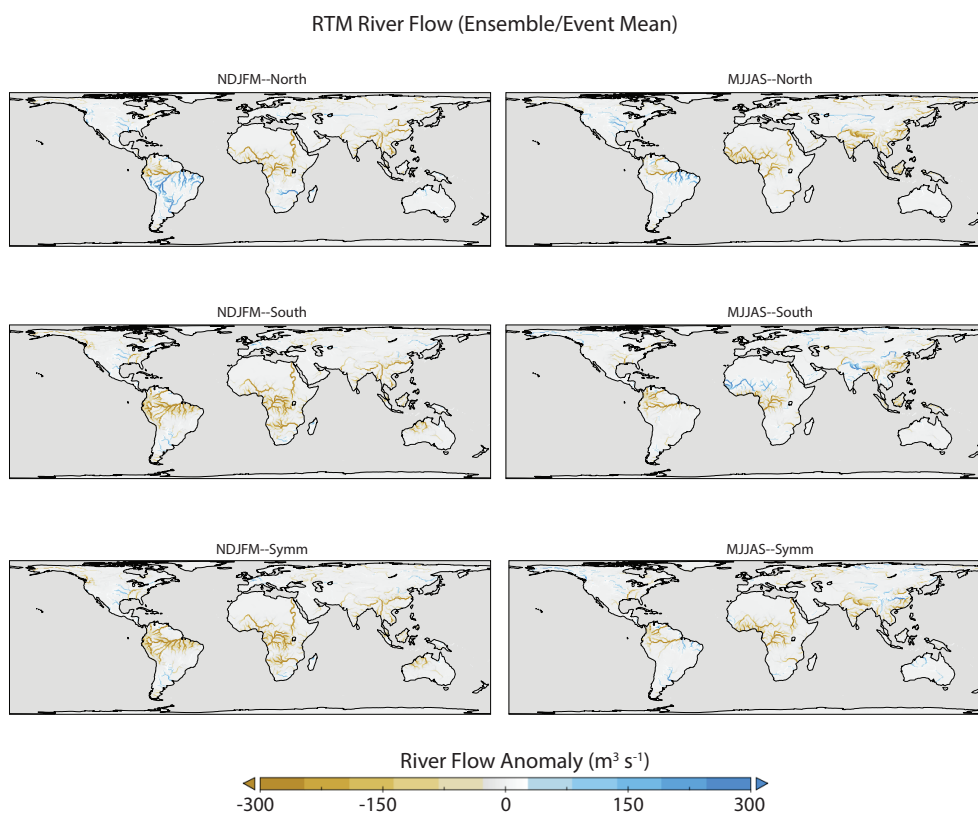
702

703 **Figure 5.** As in Figure 3, except for precipitation (mm/day, normalized to 20 Tg in the

704 forced simulations; mm/day in the control). N (not shown) is the same as in Figure 3.

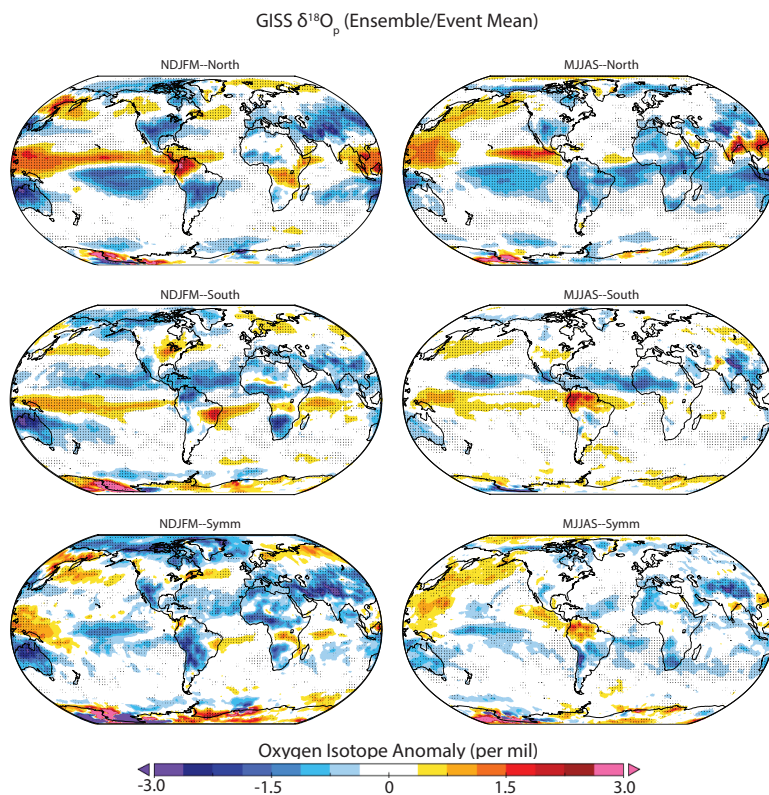


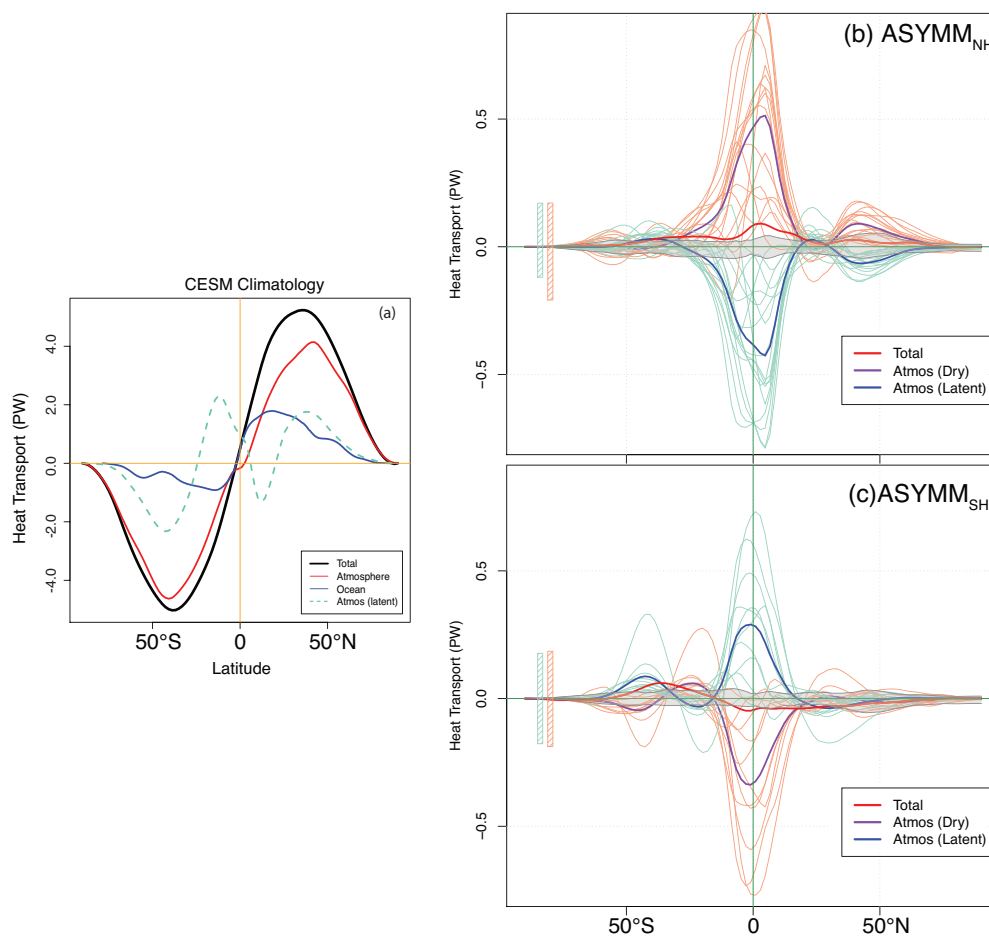
705



706

707 **Figure 6.** As in Figures 2 and 4, except for river discharge ( $\text{m}^3/\text{s}$ , or  $10^{-6}$  Sverdrups).





712

713 **Figure 8. a)** CESM climatology of atmosphere+ocean energy transport (PW, black),

714 atmosphere only (red), ocean only (dark blue), moisture component of the atmosphere

715 (latent heat, dashed aqua). **b)** Ensemble/Eruption mean anomaly in atmospheric heat

716 transport for ASYMM<sub>NH</sub> eruptions in total (red), dry (purple), and latent (aqua)

717 components. Lighter lines associated with the dry and latent components indicate the

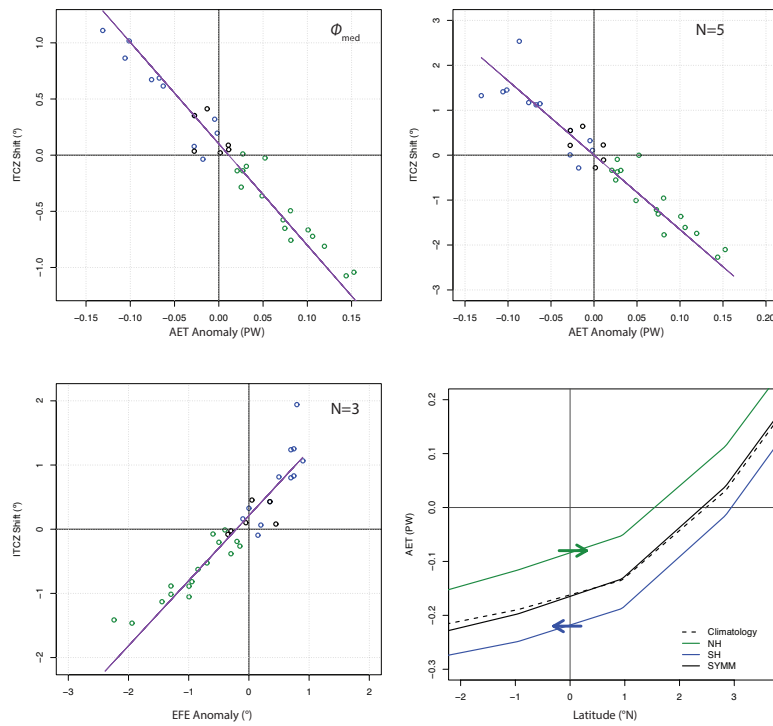
718 eruption spread, each averaged over 14 ensemble members. **c)** As in (b), except for

719 ASYMM<sub>SH</sub> eruptions. Grey envelope corresponds to the total AET anomaly vs. latitude

720 in a control simulation using 50 realizations of a composite formed from the same dates



721 as the  $ASYMM_{NH}$  results (16 “events” with no external forcing). Vertical bars correspond  
 722 to the range of (aqua) latent and (orange) dry components of  $AET_{eq}$  in the control  
 723 composite.



724  
 725 **Figure 9.** Annual-mean ITCZ shift represented by changes in (topleft)  $\phi_{med}$  and (topright)  
 726  $\phi_{ITCZ}$  ( $N = 5$ ) vs. change in  $AET_{eq}$ . (bottomleft) Changes in  $\phi_{ITCZ}$  ( $N = 3$ ) vs. change in  
 727 EFE. See text for definitions. (bottomright) Total AET vs. latitude for a small band  
 728 centered around the equator for all volcanic events in (green)  $ASYMM_{NH}$ , (blue)  
 729  $ASYMM_{SH}$ , and (black) SYMM cases. Black dashed line indicates climatological or pre-  
 730 eruption AET values (different choices are indistinguishable). Colored arrows represent  
 731 the direction of anomalous  $AET_{eq}$ .



**Table 1.** List of LM Eruptions

Eruption Category	Seasons in LM Composite (MJJAS)	Seasons in LM Composite (NDJFM)
ASYMM <sub>NH</sub>	870, 901, 933/934, 1081, 1176/1177, 1213/1214, 1328, 1459, 1476, 1584, 1600/1601, 1641/1642, 1719/1720, 1762/1763, 1831, 1835/1836	871, 902, 934, 1082, 1177, 1214/1215, 1329, 1460, 1585, 1601, 1641/1642, 1720, 1730, 1762/1763, 1832, 1835/1836
ASYMM <sub>SH</sub>	929, 961, 1158.5/1159.5, 1232, 1268, 1275/1276, 1341/1342, 1452/1453, 1593, 1673, 1693/1694	962, 1159, 1233, 1269, 1276/1277, 1285, 1342, 1453/1454, 1674, 1694
SYMM	854, 1001, 1284/1285, 1416, 1809/1810, 1815/1816	855, 1002, 1810, 1816/1817

- 732 1) Dates of Eruption events used in composite results, based on reconstructed stratospheric sulfate  
 733 loadings from Gao et al. (2008).  
 734 2) Combined dates with a “/” indicate a multi-season event where every inclusive month is first averaged  
 735 prior to entering the multi-eruption composite.



736 **References**

737

738 Adam, O., Bischoff, T., and Schneider, T.: Seasonal and interannual variations of the  
739 energy flux equator and ITCZ, Part I: Zonally averaged ITCZ position, *J. Climate*, in  
740 press.

741 Allen, R. J., Evan, A. T., and Booth, B. B.: Interhemispheric aerosol radiative forcing and  
742 tropical precipitation shifts during the late twentieth century, *J. Climate*, 28, 8219–  
743 8246, doi:10.1175/JCLI-D-15-0148.1, 2015.

744 Araguás-Araguás, L., Froehlich, K., and Rozanski, K.: Deuterium and oxygen-18 isotope  
745 composition of precipitation and atmospheric moisture, *Hydrol. Process.*, 14, 1341–  
746 1355, doi: 10.1002/1099-1085(20000615)14:8<1341::AID-HYP983>3.0.CO;2-Z,  
747 2000.

748 Atwood, A., Wu, E., Frierson, D. M. W., Battisti, D., and Sachs, J. P.: Quantifying  
749 Climate Forcings and Feedbacks over the Last Millennium in the CMIP5–PMIP3  
750 Models, *J. Climate*, 29, 1161–1178, doi: 10.1175/JCLI-D-15-0063.1, 2016.

751 Bischoff, T., and Schneider, T.: Energetic constraints on the position of the Intertropical  
752 Convergence Zone, *J. Climate*, 27, 4937–4951, doi:10.1175/JCLI-D-13-00650.1,  
753 2014.

754 Broccoli, A. J., Dahl, K. A., and Stouffer, R. J.: Response of the ITCZ to Northern  
755 Hemisphere cooling, *Geophys. Res. Lett.*, 33, L01702, doi:10.1029/2005GL024546,  
756 2006.

757 Chiang, J. C. H., and Bitz, C. M.: Influence of high latitude ice cover on the marine  
758 Intertropical Convergence Zone, *Clim. Dyn.*, 25, 477– 496, doi:10.1007/s00382-005-  
759 0040-5, 2005.

760 Chiang, J. C. H., and Friedman, A. R.: Extratropical Cooling, Interhemispheric Thermal



- 761 Gradients, and Tropical Climate Change, *Ann. Rev. Earth Plan. Sci.*, 40, 383-412,  
762 doi:10.1146/annurev-earth-042711-105545, 2012.
- 763 Colose, C. M., LeGrande, A. N., and Vuille, M.: The influence of volcanic eruptions on  
764 the climate of tropical South America during the last millennium in an isotope-  
765 enabled general circulation model, *Clim. Past*, 12, 961-979, doi:10.5194/cp-12-961-  
766 2016, 2016.
- 767 Crowley, T. J. and Unterman, M. B.: Technical details concerning development of a  
768 1200-yr proxy index for global volcanism, *Earth Syst. Sci. Data*, 5, 187–197,  
769 doi:10.5194/essd-5-187-2013, 2013.
- 770 Dansgaard, W.: Stable isotopes in precipitation, *Tellus*, 16, 436–468, doi:10.1111/j.2153-  
771 3490.1964.tb00181.x, 1964.
- 772 Deser, C., Phillips, A. S., Bourdette, V., and Teng, H.: Uncertainty in climate change  
773 projections: The role of internal variability, *Clim. Dyn.*, 38, 527–546,  
774 doi:10.1007/s00382-010-0977-x, 2012.
- 775 Donohoe, A., Marshall, J., Ferreira, D., and McGee, D.: The relationship between ITCZ  
776 location and cross-equatorial atmospheric heat transport: From the seasonal cycle to  
777 the last glacial maximum, *J. Climate*, 26, 3597–3618, doi:10.1175/JCLI-D-12-  
778 00467.1, 2013.
- 779 Fasullo, J. T., and Trenberth, K. E.: The annual cycle of the energy budget. Part II:  
780 Meridional structures and poleward transports, *J. Climate*, 21, 2313–2325,  
781 doi:10.1175/2007JCLI1936.1, 2008.



- 782 Friedman, A. R., Hwang, Y.-T., Chiang, J. C. H., and Frierson, D. M. W.: The  
783 interhemispheric thermal gradient over the 20th century and in future projections, *J.*  
784 *Climate*, 26, 5419-5433, doi: 10.1175/JCLI-D-12-00525.1, 2013.
- 785 Frierson, D. M. W., and Hwang, Y.-T.: Extratropical influence on ITCZ shifts in slab  
786 ocean simulations of global warming, *J. Climate*, 25, 720–733, doi:10.1175/JCLI-D-  
787 11-00116.1, 2012.
- 788 Frierson, D. M. W., Hwang, Y.-T., Fuckar, N. S., Seager, R., Kang, S. M., Donohoe, A.,  
789 Maroon, E. A., Liu, X., and Battisti, D. S.: Contribution of ocean overturning  
790 circulation to tropical rainfall peak in the Northern Hemisphere, *Nat. Geosci.*, 6, 940–  
791 944, doi:10.1038/ngeo1987, 2013.
- 792 Gao, C., Robock, A., and Ammann, C.: Volcanic forcing of climate over the past 1500  
793 years: An improved ice core-based index for climate models, *J. Geophys. Res.*  
794 *Atmos.*, 113, D23111, doi:10.1029/2008JD010239, 2008.
- 795 Haywood, J. M., Jones, A., Bellouin, N., and Stephenson, D.: Asymmetric forcing from  
796 stratospheric aerosols impacts Sahelian rainfall, *Nat. Clim. Change*, 3, 660–665,  
797 doi:10.1038/NCLIMATE1857, 2013.
- 798 Hurrell, J. W., et al., The Community Earth System Model: A framework for  
799 collaborative research, *Bull. Am. Meteorol. Soc.*, 94, 1339–1360,  
800 doi:10.1175/BAMS-D-12-00121, 2013.
- 801 Hwang, Y.-T., and Frierson, D. M. W.: Link between the double-Intertropical  
802 Convergence Zone problem and cloud biases over the Southern Ocean, *Proc. Natl.*  
803 *Acad. Sci.*, 110, 4935–4940, doi:10.1073/pnas.1213302110, 2013.
- 804 Hwang, Y.-T., Frierson, D. M. W., and Kang, S. M.: Anthropogenic sulfate aerosol and



- 805 the southward shift of tropical precipitation in the 20th century, *Geophys. Res. Lett.*,  
806 40, 1–6, doi: 10.1002/grl50502, 2013.
- 807 Iles, C. E., Hegerl, G. C., Schurer, A. P., and Zhang, X.: The effect of volcanic eruptions  
808 on global precipitation, *J. Geophys. Res. Atmos.*, 118, 8770–8786,  
809 doi:10.1002/jgrd.50678, 2013.
- 810 Iles, C. E., and Hegerl, G. C., The global precipitation response to volcanic eruptions in  
811 the CMIP5 models, *Environ. Res. Lett.*, 9, 104012, doi:10.1088/1748-  
812 9326/9/10/104012, 2014.
- 813 Kang, S. M., Held, I. M., Frierson, D. M. W., and Zhao, M.: The response of the ITCZ to  
814 extratropical thermal forcing: Idealized slab ocean experiments with a GCM, *J.*  
815 *Climate*, 21, 3521–3532, doi:10.1175/2007JCLI2146.1, 2008.
- 816 Kang, S. M., Frierson, D. M. W., and Held, I. M.: The tropical response to extratropical  
817 thermal forcing in an idealized GCM: The importance of radiative feedbacks and  
818 convective parameterization, *J. Atmos. Sci.*, 66, 2812–2827,  
819 doi:10.1175/2009JAS2924.1, 2009.
- 820 Kang, S. M., Seager, R., Frierson, D. M. W., and Liu, X.: Croll revisited: Why is the  
821 northern hemisphere warmer than the southern hemisphere?, *Clim. Dyn.*, 44, 1457–  
822 1472, doi:10.1007/s00382-014-2147-z, 2014.
- 823 Kravitz, B., and Robock, A.: Climate effects of high-latitude volcanic eruptions: Role of  
824 the time of year, *J. Geophys. Res.*, 116, D01105, doi:10.1029/2010JD014448, 2011.
- 825 Lacis, A., Hansen, J. and Sato, M.: Climate forcing by stratospheric aerosols, *Geophys.*  
826 *Res. Lett.*, 19, 1607–1610, doi:10.1029/92GL01620, 1992.
- 827 Lacis, A.: Volcanic aerosol radiative properties, *PAGES Newsletter*, 23, 2, 50–51, 2015.



- 828 LeGrande, A.N., and Schmidt, G.A.: Ensemble, water-isotope enabled, coupled general  
829 circulation modeling insights into the 8.2-kyr event, *Paleoceanogr.*, 23, PA3207,  
830 doi:10.1029/2008PA001610, 2008.
- 831 LeGrande, A.N., and Schmidt, G.A.: Sources of Holocene variability of oxygen isotopes  
832 in paleoclimate archives, *Clim. Past*, 5, 441-455, doi:10.5194/cp-5-441-2009, 2009.
- 833 LeGrande, A.N., and Anchukaitis, K. J.: Volcanic eruptions and climate, *PAGES*  
834 *Newsletter*, 23, 2, 46-47, 2015.
- 835 Liu, F., Chai, J., Wang, B., Liu, J., Zhang, X., Wang, Z.: Global monsoon precipitation  
836 responses to large volcanic eruptions, *Sci. Rep.*, 6, 24331, doi: 10.1038/srep24331,  
837 2016.
- 838 Mann, G., Dhomse, S., Deshler, T., Timmreck, C., Schmidt, A., Neely, R., and  
839 Thomason, L.: Evolving particle size is the key to improved volcanic forcings,  
840 *PAGES Newsletter.*, 23, 2, 52-53, 2015.
- 841 Maroon, E. A., Frierson, D. M. W., Kang, S. M., and Scheff, J.: The precipitation  
842 response to an idealized subtropical continent, *J. Climate*, doi:10.1175/JCLI-D-15-  
843 0616.1, in press.
- 844 Marshall, J., Donohoe, A., Ferreira, D., and McGee, D.: The ocean's role in setting the  
845 mean position of the Intertropical Convergence Zone, *Clim. Dyn.*, 42, 1967–1979,  
846 doi:10.1007/s00382-013-1767-z, 2013.
- 847 McGee, D., A. Donohoe, J. Marshall, D. Ferreira, Changes in ITCZ location and cross-  
848 equatorial heat transport at the Last Glacial Maximum, Heinrich Stadial 1, and the  
849 mid-Holocene, *Earth Plan. Sci. Lett.*, 390, 69-79, doi:10.1016/j.epsl.2013.12.043,  
850 2014.



- 851 Miller, R.L., et al., CMIP5 historical simulations (1850-2012) with GISS-E2 ModelE2. J.  
852 Adv. Model. Earth Syst., 6(2), 441-477, doi:10.1002/2013MS000266, 2014.
- 853 Neelin, J. D. and Held, M.: Modeling tropical convergence based on the moist static  
854 energy budget, Mon. Wea. Rev., 115, 3-12, doi: 10.1175/1520-  
855 0493(1987)115<0003:MTCBOT>2.0.CO;2, 1987.
- 856 Oleson, K. W., et al., Technical description of version 4.0 of the Community Land Model  
857 (CLM), NCAR Tech. Note NCAR/TN-478+STR, 257 pp., Natl. Cent. for Atmos.  
858 Res., Boulder, Colo, 2010.
- 859 Oman, L., Robock, A., Stenchikov, G., Schmidt, G. A., and Ruedy, R.: Climatic response  
860 to high latitude volcanic eruptions, J. Geophys. Res, 110, D13103,  
861 doi:10.1029/2004JD005487, 2005.
- 862 Oman, L., Robock, A., Stenchikov, G. L., and Thordarson, T.: High-latitude eruptions  
863 cast shadow over the African monsoon and the flow of the Nile, Geophys. Res. Lett.,  
864 33, L18711, doi:10.1029/2006GL027665, 2006.
- 865 Ortega, P., Lehner, F., Swingedouw, D., Masson-Delmotte, V., Raible, C. C., Casado,  
866 M., and Yiou, P.: A model-tested North Atlantic Oscillation reconstruction for the  
867 past millennium, Nature, 523, 71–74, doi:10.1038/nature14518, 2015.
- 868 Otto-Bliesner, B. L., Brady, E. C., Fasullo, J., Jahn, A., Landrum, L., Stevenson, S.,  
869 Rosenbloom, N., Mai, A., and Strand, G.: Climate Variability and Change since 850  
870 C.E, Climate variability and change since 850 C.E.: An ensemble approach with the  
871 Community Earth System Model (CESM), Bull. Am. Meteorol. Soc.,  
872 doi:10.1175/BAMS-D-14-00233.1, 2016, in press.
- 873 Oueslati, B., and Bellon, G., The double ITCZ bias in CMIP5 models: interaction



- 874 between SST, large-scale circulation and precipitation, *Clim. Dyn.*, 44, 585-607,  
875 doi:10.1007/s00382-015-2468-6, 2015.
- 876 Pausata, F. S. R., Chafik, L., Caballero, R., and Battisti, D. S.: Impacts of a high-latitude  
877 volcanic eruption on AMOC and ENSO, *Proc. Nat. Acad. Sci.*, 112, 13784-13788,  
878 doi: 10.1073/pnas.1509153112, 2015.
- 879 Ridley, H. E., et al., Aerosol forcing of the position of the intertropical convergence zone  
880 since AD 1550, *Nat. Geosci.*, 8, 195-200, doi:10.1038/ngeo2353, 2015.
- 881 Robock, A. and Mao, J.: Winter warming from large volcanic eruptions, *Geophys. Res.*  
882 *Lett.*, 19, 2405-2408, doi:10.1029/92GL02627, 1992.
- 883 Robock, A. and Mao, J.: The volcanic signal in surface temperature observations. *J.*  
884 *Climate*, 8, 1086-1103, doi:10.1175/1520-0442(1995)008<1086:TVSIST>2.0.CO;2,  
885 1995.
- 886 Robock, A., Volcanic eruptions and climate, *Rev. Geophys.*, 38, 191–219,  
887 doi:10.1029/1998RG000054, 2000.
- 888 Sato, M., Hansen, J. E., McCormick, M. P., and Pollack, J. B.: Stratospheric aerosol  
889 optical depths, 1850-1990, *J. Geophys. Res.*, 98, 22987-22994,  
890 doi:10.1029/93JD02553, 1993.
- 891 Schmidt, G. A., Hoffmann, G., Shindell, D. T., and Hu, Y.: Modeling atmospheric stable  
892 water isotopes and the potential for constraining cloud processes and stratosphere-  
893 troposphere water exchange, *J. Geophys. Res.*, 110, D21314,  
894 doi:10.1029/2005JD005790, 2005.
- 895 Schmidt, G. A., LeGrande, A. N., and Hoffmann, G.: Water isotope expressions of  
896 intrinsic and forced variability in a coupled ocean-atmosphere model, *J. Geophys.*



- 897 Res., 112, D10103, doi:10.1029/2006JD007781, 2007.
- 898 Schmidt, G.A., et al., , Climate forcing reconstructions for use in PMIP simulations of the  
899 last millennium (v1.0), *Geosci. Model Dev.*, 4, 33-45, doi:10.5194/gmd-4-33-2011,  
900 2011.
- 901 Schneider, T., Bischoff, T., and Haug, G. H.: Migrations and dynamics of the  
902 Intertropical Convergence Zone, *Nature*, 513, 45–53, doi:10.1038/nature13636, 2014.
- 903 Shindell, D. T., Schmidt, G. A., Mann, M. E., and Faluvegi, G.: Dynamic winter climate  
904 response to large tropical volcanic eruptions since 1600, *J. Geophys. Res.*, 109,  
905 D05104, doi:10.1029/2003JD004151, 2004.
- 906 Sigl, M., et al. , Timing and climate forcing of volcanic eruptions for the past 2,500 years,  
907 *Nature*, 523, 543-549, doi:10.1038/nature14565, 2015.
- 908 Stenchikov, G., Robock, A., Ramaswamy, V., Schwarzkopf, M. D., Hamilton, K., and  
909 Ramachandran, S.: Arctic Oscillation response to the 1991 Mount Pinatubo eruption,  
910 Effects of volcanic aerosols and ozone depletion, *J. Geophys. Res.*, 107, 4803,  
911 doi:10.1029/2002JD002090, 2002.
- 912 Stothers, R. B.: The Great Tambora Eruption in 1815 and its aftermath, *Science*, 224,  
913 1191–1198, doi:10.1126/science.224.4654.1191, 1984.
- 914 Trenberth, K. E., and Dai, A.: Effects of Mount Pinatubo volcanic eruption on the  
915 hydrological cycle as an analog of geoengineering, *Geophys. Res. Lett.*, 34, L15702,  
916 doi:10.1029/2007GL030524, 2007.
- 917 Trenberth, K. E., and Caron, J. M.: Estimates of meridional atmosphere and ocean heat  
918 transports, *J. Climate*, 14, 3433-3443, doi:10.1175/1520-  
919 0442(2001)014<3433:EOMAAO>2.0.CO;2, 2001.



- 920 Vuille, M., Bradley, R. S., Werner, M., Healy, R., and Keimig, F.: Modeling  $d^{18}O$  in  
921 precipitation over the tropical Americas: 1. Interannual variability and climatic  
922 controls, *J. Geophys. Res.*, 108, D6, 4174, doi:10.1029/2001JD002038, 2003.
- 923 Wunsch, C., The total meridional heat flux and its oceanic and atmospheric partition, *J.*  
924 *Climate*, 18, 4374–4380, doi:10.1175/JCLI3539.1, 2005.
- 925 Yoshimori, M., and Broccoli, A. J.: Equilibrium response of an atmosphere-mixed layer  
926 288 ocean model to different radiative forcing agents: Global and zonal mean  
927 response, *J. Climate*, 21, 4399–4423, doi:10.1175/2008jcli2172.1, 2008.
- 928 Yoshimori, M., and Broccoli, A. J.: On the link between Hadley circulation changes and  
929 radiative feedback processes, *Geophys. Res. Lett.*, 36, L20703,  
930 doi:10.1029/2009GL040488, 2009.
- 931
- 932
- 933